

Supplementary Information

Controllable Synthesis of Layered Antiferromagnetic Oxyhalide CrOCl via Chemical Vapor Deposition

Rounak Banerjee^{1,2,#}, Sai Uppala^{1,#}, Jan Kopaczek^{1,3}, Sakib Ahmed⁴, Cheng-Lun Wu¹, Mukesh Kumar¹, Kentaro Yumigeta^{1,5}, Umberto Celano⁴ and Seth Ariel Tongay^{1,*}

¹Materials Science and Engineering, School for Engineering of Matter, Transport and Energy, Arizona State University, Tempe, AZ 85287, USA

²Department of Physics, College of Liberal Arts and Sciences, Arizona State University, Tempe, AZ 85287, USA

³Department of Semiconductor Materials Engineering, Faculty of Fundamental Problems of Technology, Wrocław University of Science and Technology, Wybrzeże Wyspiańskiego 27, Wrocław, 50-370 Poland

⁴School of Electrical, Computer and Energy Engineering, Arizona State University, Tempe, AZ 85287, USA

⁵Materials Science and Engineering Department, University of Arizona, Tucson, AZ, USA

These authors contributed equally to this work.

*Corresponding author: stongay@asu.edu

Figures

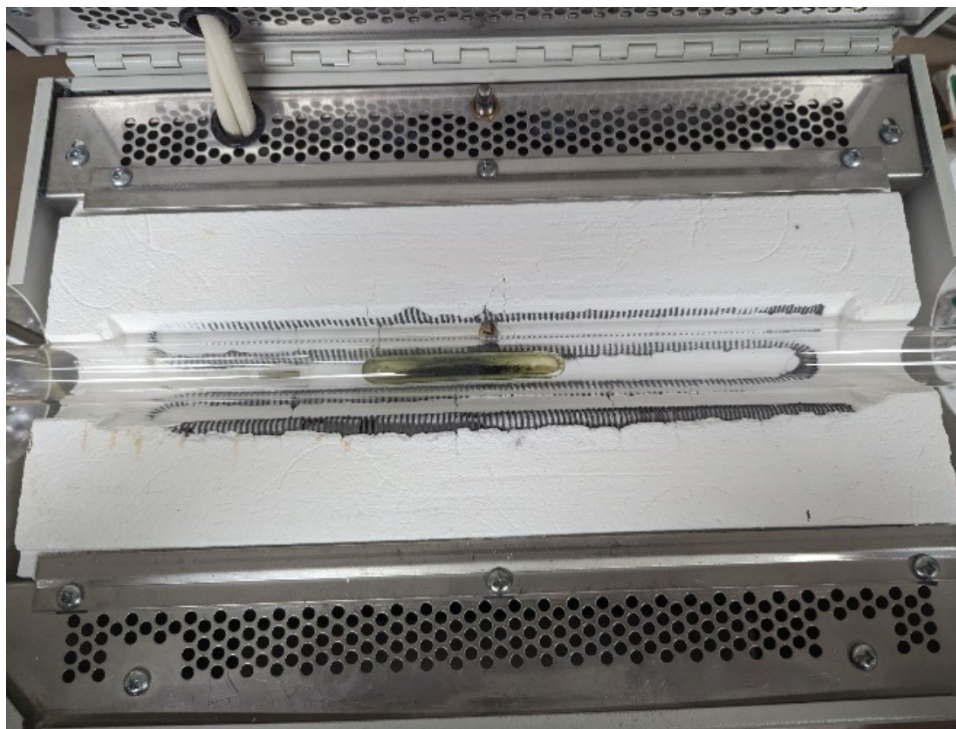


Figure S1: Furnace with quartz boat containing precursors. In this example, the boat turned green due to the formation of Cr_2O_3 at high growth temperature ($\sim 850^\circ\text{C}$) while passing O_2 gas over the CrCl_3 precursor.

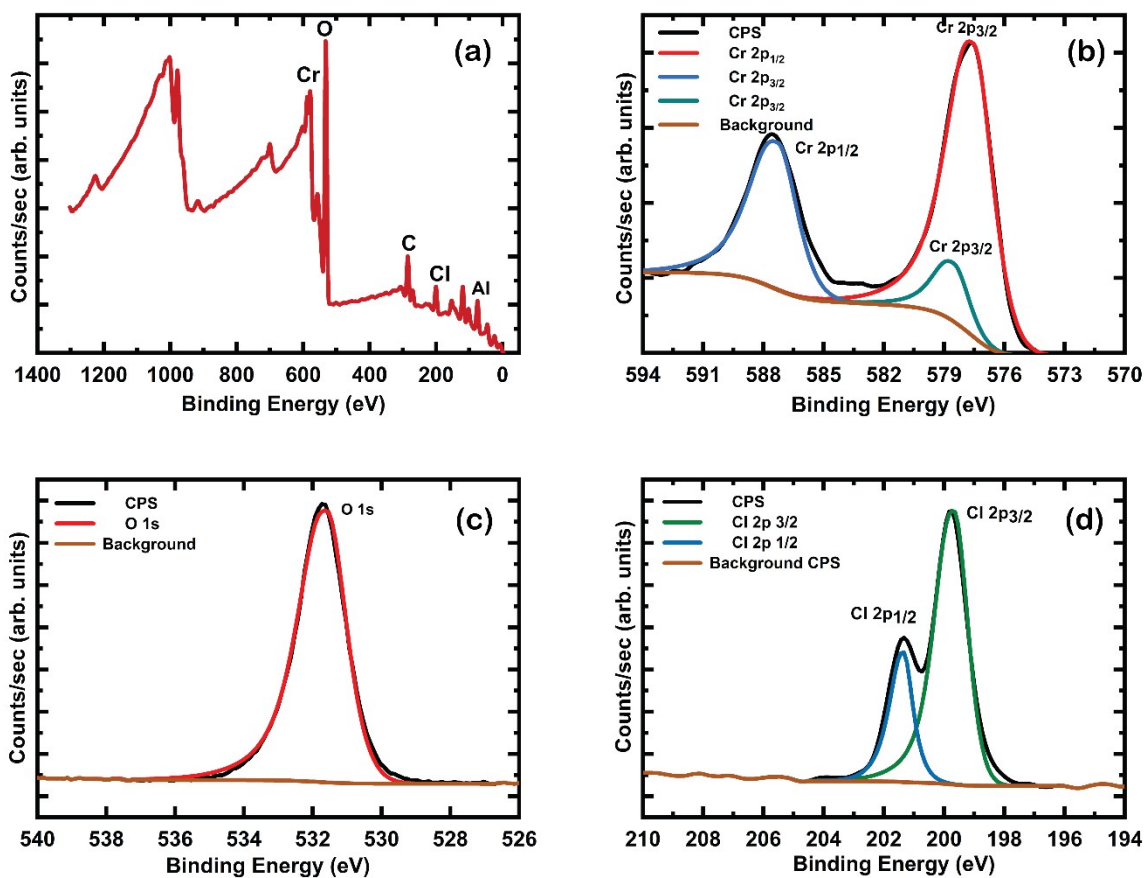


Figure S2: X-ray photoelectron Spectroscopy (XPS) of CrOCl grown via APCVD on sapphire substrates. Wide (a) and elemental (b-d) scans confirm the stoichiometry of the thin sheets.

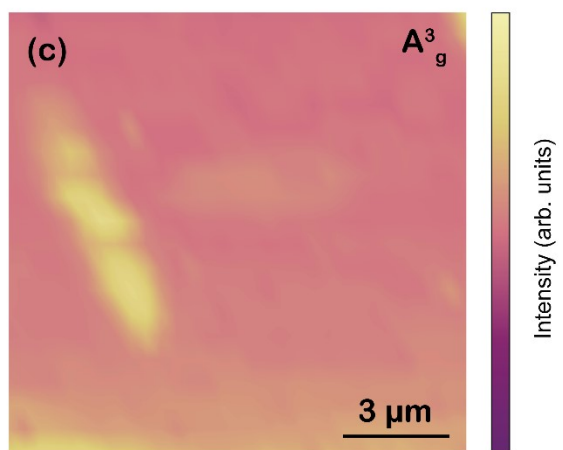
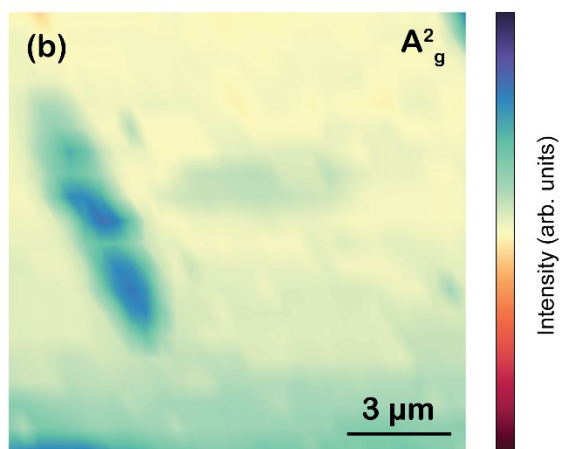
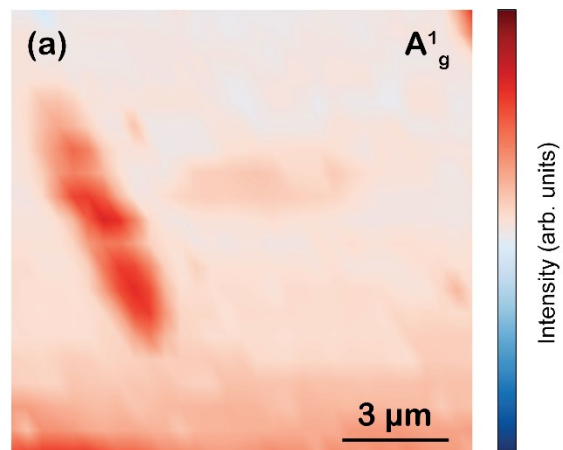


Figure S3: Raman Mapping of APCVD grown CrOCl sheets corresponding to the three Raman modes A^1_g , A^2_g , and A^3_g .

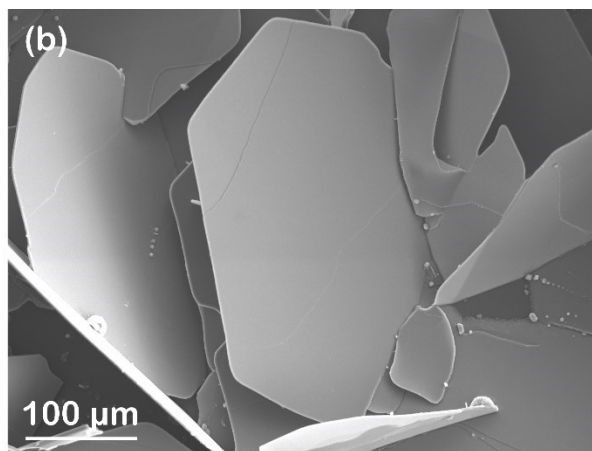
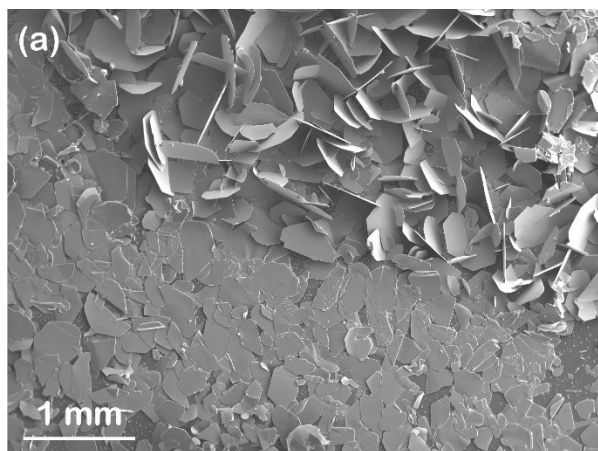


Figure S4: Large area SE image of the substrate when growth is done with O_2 deficit. (a) The large flakes at the top right corner of the substrate are $CrCl_3$. (b) Magnified SE image of $CrCl_3$ deposited via APCVD.

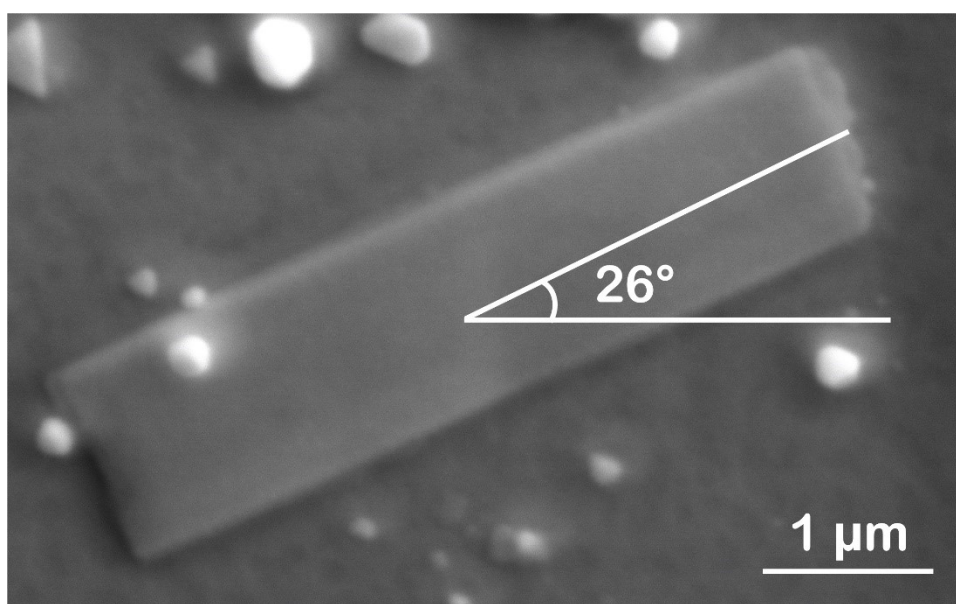


Figure S5: Secondary Electron (SE) image of flake used for Angle-Resolved Raman Spectra

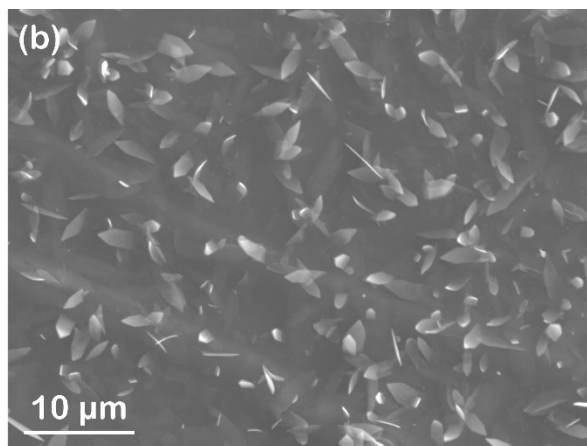
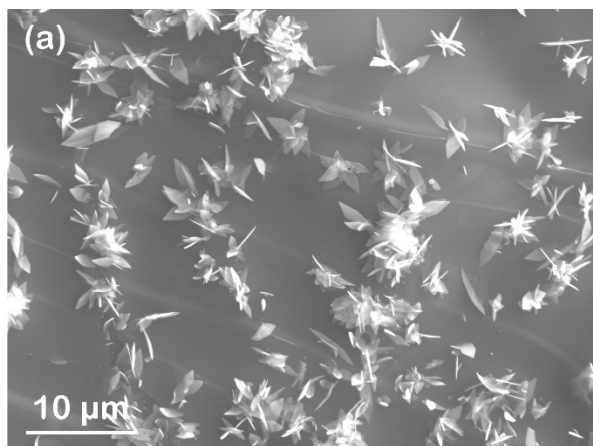


Figure S6: Large area SE images of mica substrates showing out-of-plane CrOCl growth. Distinct flower-like patterns (a) become more planar (b) as carrier gas flow rate is altered from 5 to 12.5 sccm.

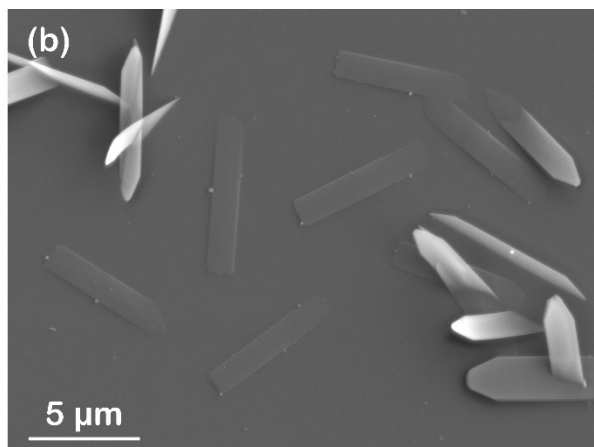
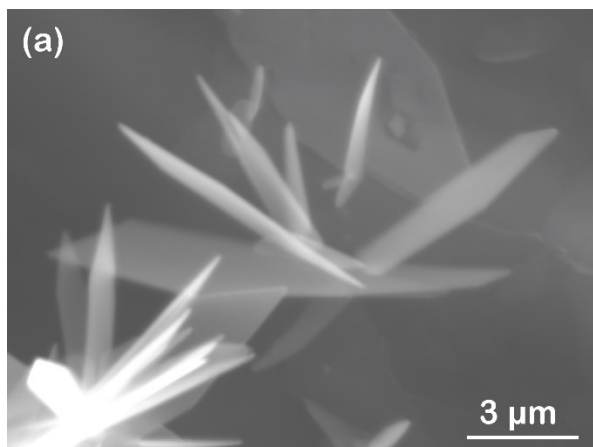


Figure S7: Magnified SE images of platelet-like out-of-plane growths on sapphire substrates.

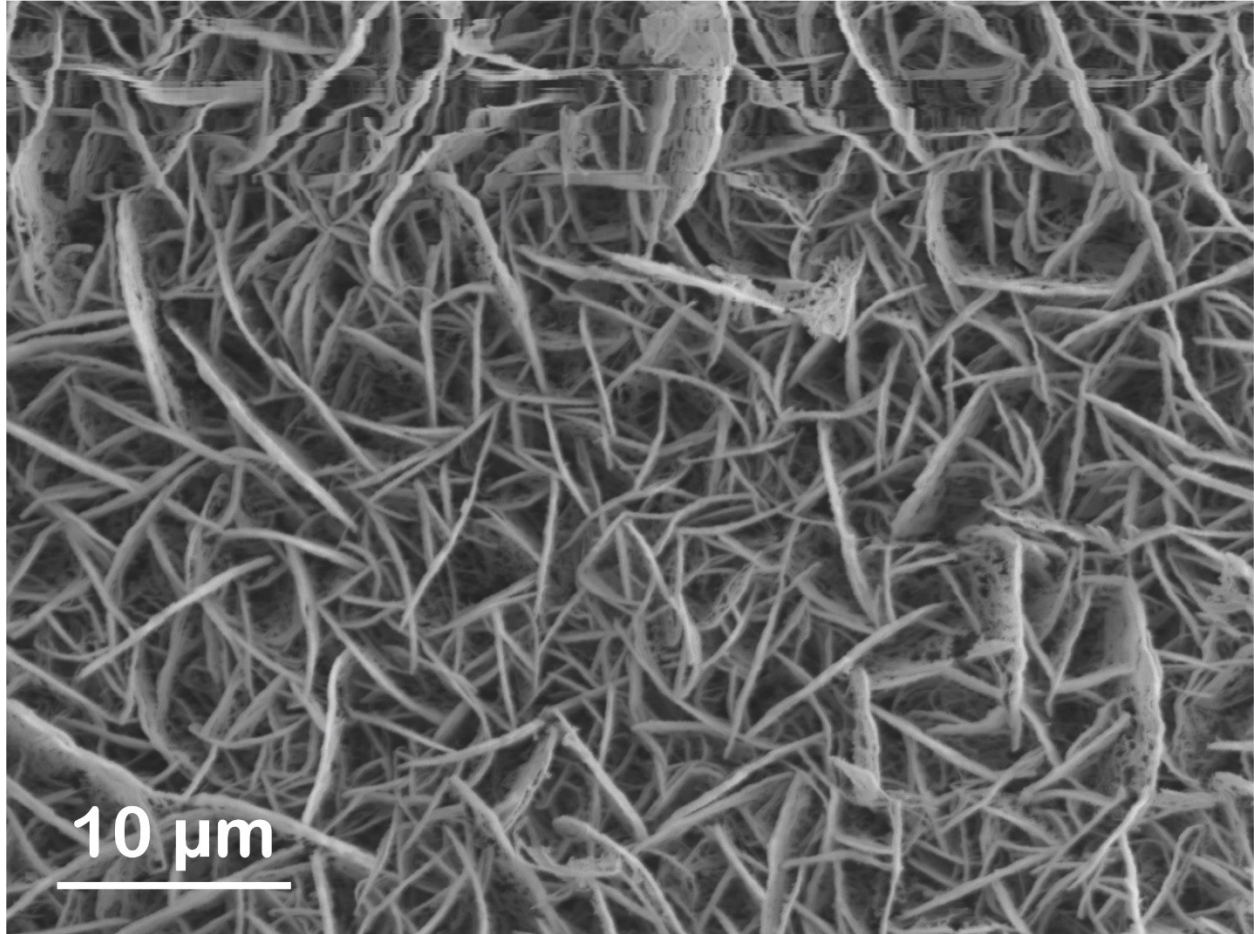


Figure S8: Dense substrate coverage of CrOCl for low pressure (LPCVD) growth at pressure ~100 mtorr.

Raman Spectra and Vibration Modes of CrOCl

CrOCl has an orthorhombic crystal structure belonging to the Pmmn space group with D_{2h} point group symmetry²¹. In the irreducible representation, the phonon modes are represented as

$$\Gamma = 3 A_g + 3 B_{2g} + 3 B_{3g} + 3 B_{1u} + 3 B_{2u} + 3 B_{3u}$$

Out of these, only the A_g and B_g modes are Raman active, while the B_u modes are IR active.

The Raman intensity is given by

$I = |e_s \cdot R_x \cdot e_i|^2$, where I is the Raman intensity, R_x is the Raman tensor of mode x , and e_s and e_i are the electric field vectors of scattered and incident light.

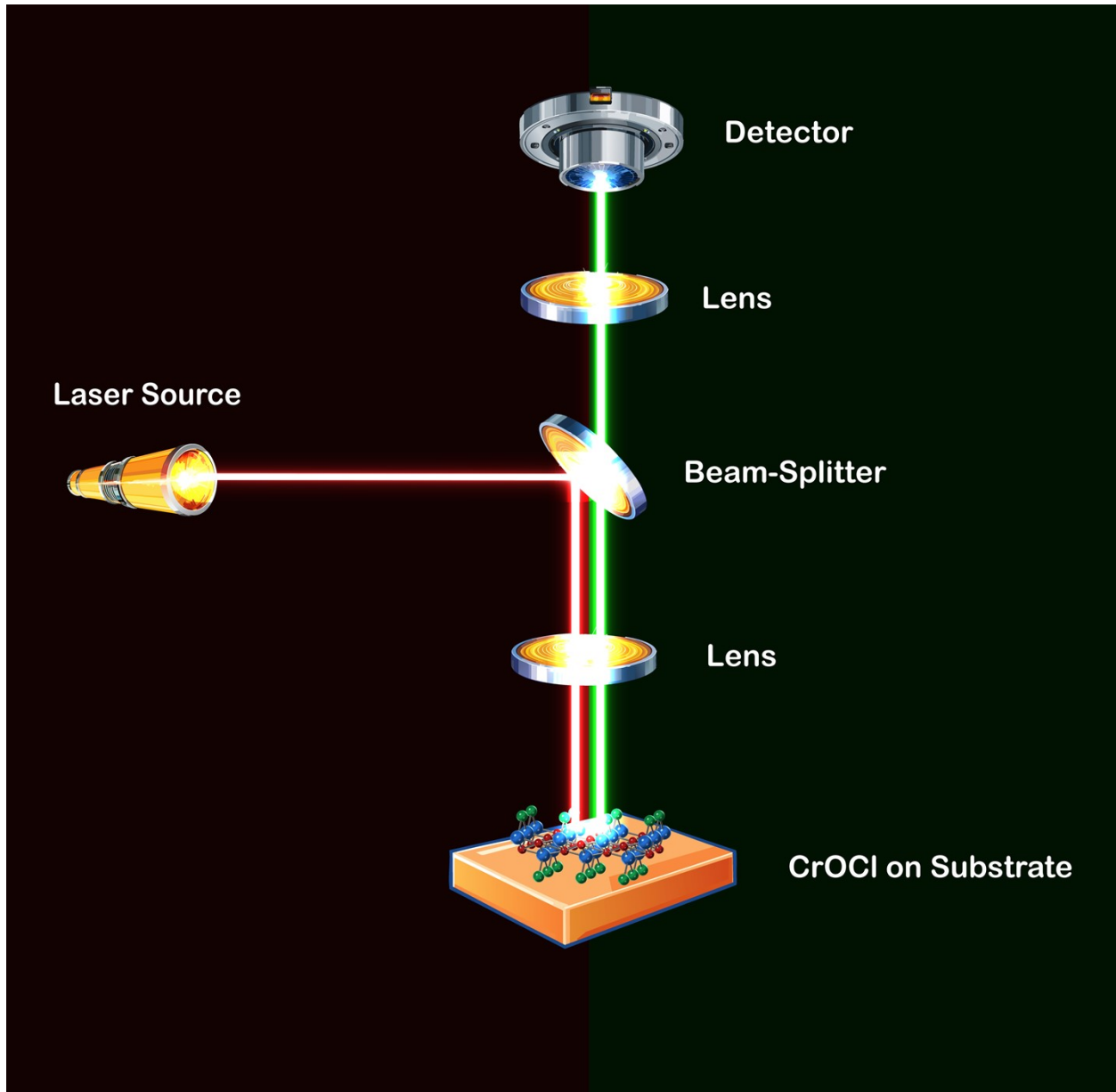


Figure S9: Schematic depiction of the experimental setup for collecting Raman spectra in backscattering geometry.

The Raman tensor for A_g mode has the form,

$$R_{A_g} = \begin{pmatrix} a & 0 & 0 \\ 0 & b & 0 \\ 0 & 0 & c \end{pmatrix}, \text{ thus, the Raman intensity becomes}$$

$$I(A_g) = \left| \begin{pmatrix} \cos \theta \\ \sin \theta \\ 0 \end{pmatrix} \cdot \begin{pmatrix} a & 0 & 0 \\ 0 & b & 0 \\ 0 & 0 & c \end{pmatrix} \cdot \begin{pmatrix} \cos \theta \\ \sin \theta \\ 0 \end{pmatrix} \right|^2 = (a \cos^2 \theta + b \sin^2 \theta)^2$$

This has an intensity variation with a period of 180° , in accordance with what we find in Figure 4a-c. The offset from 0 is because of the initial angle of the flake from the polarization direction as shown in Figure S5.

Furthermore, the Raman tensor for the B_g modes have the general form

$$R_{B_g} = \begin{pmatrix} 0 & 0 & d \\ 0 & 0 & 0 \\ d & 0 & 0 \end{pmatrix} \text{ or } \begin{pmatrix} 0 & 0 & 0 \\ 0 & 0 & e \\ 0 & e & 0 \end{pmatrix}, \text{ in which the diagonal elements are 0, hence the final Intensity } I(B_g) = 0$$

Thus, due to symmetry considerations, our measurement in backscattering Raman configuration (Figure S9) only allows us to observe the 3 A_g modes labeled A_{1g} , A_{2g} , and A_{3g} .

The individual vibration modes for these 3 A_g modes are shown in Figure S10 (From supplementary information in Ref 13).

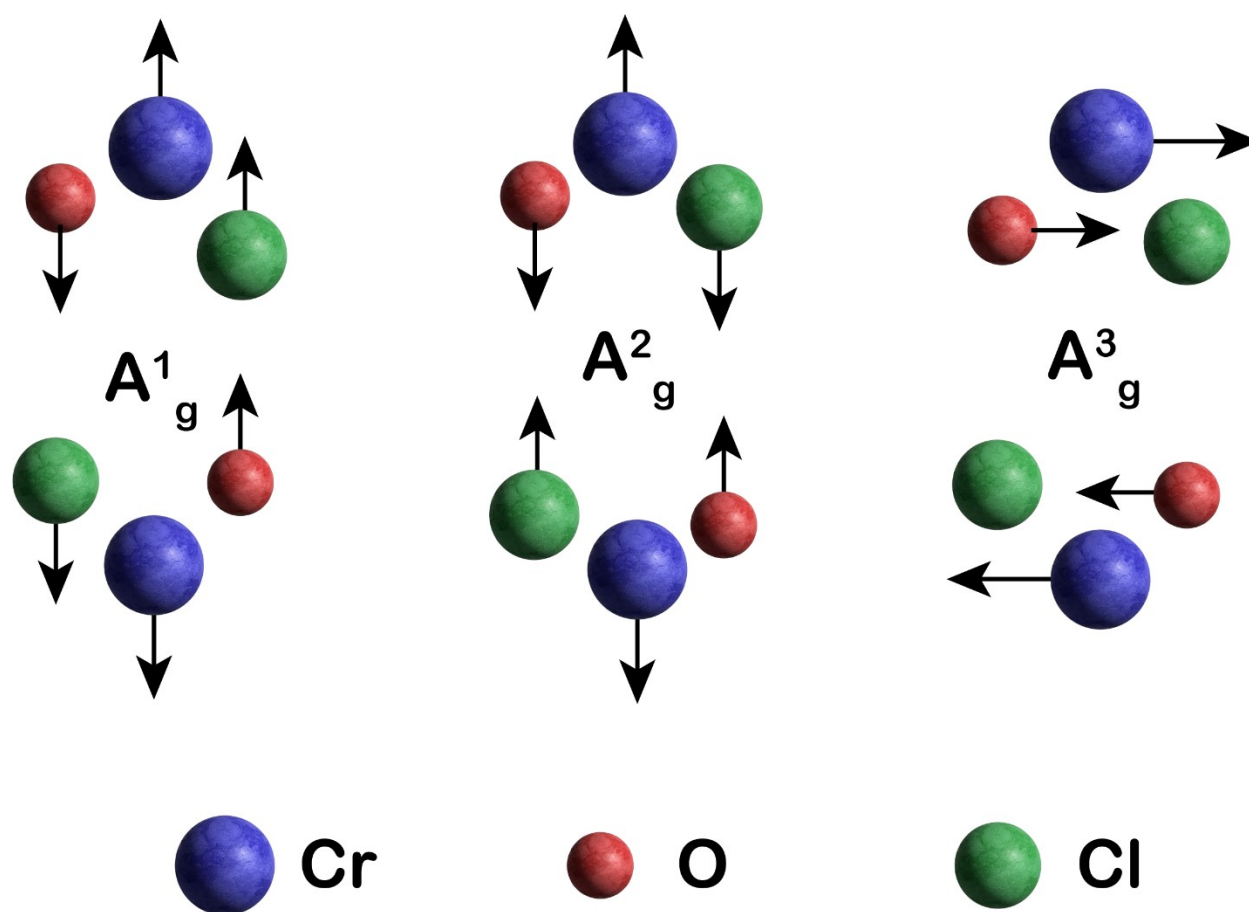


Figure S10: Schematic depiction of the three Raman vibration modes A_{1g} , A_{2g} and A_{3g} .

Ambient Stability of CrOCl

Additional measurements were conducted to demonstrate the ambient stability of the CrOCl flakes. Figure S11 shows optical images of the CVD-grown crystals captured immediately after synthesis and again eight months later, with no visible degradation.

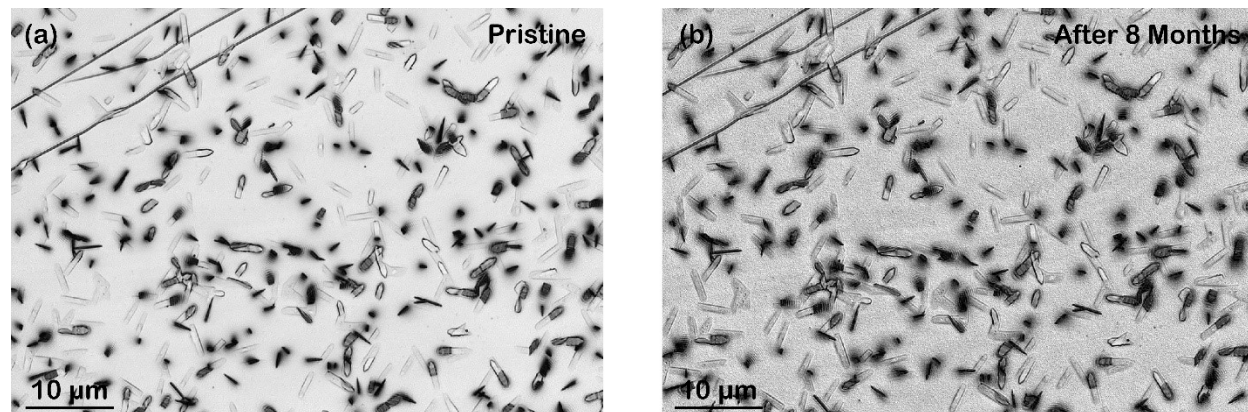


Figure S11: Optical images of CVD-grown CrOCl in (a) pristine condition and (b) after 8 months

Figure S12 presents Raman spectra of these crystals, comparing the Raman intensities over time and showing no significant changes between the spectra collected at different intervals. Additionally, SEM and EDS mapping of the crystals confirm the compositional uniformity over the eight-month period. These findings collectively confirm the long-term stability of the studied material under ambient conditions.

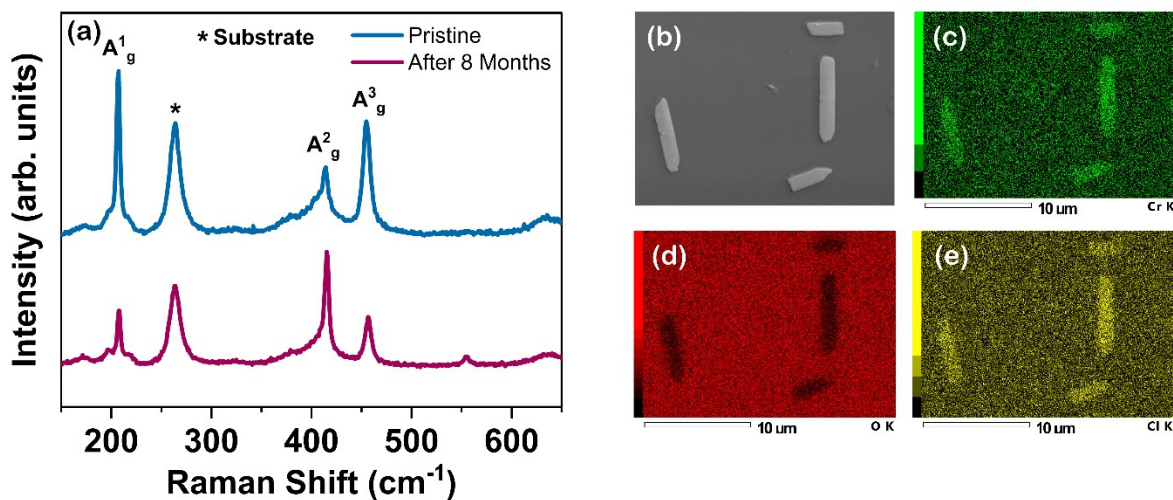


Figure S12: (a) Raman Spectra of CrOCl in Pristine condition vs after 8 months (b-e) SE Images of CVD grown flakes after 8 months showing uniformity in composition

Formula	Mass%	Atom%	Sigma	K ratio	Line
O	14.05	31.02	0.09	0.7590443	K
Cl	33.34	33.23	0.11	3.9123007	K
Cr	52.61	35.75	0.24	5.7615712	K
Total	100.00	100.00			

Magnetism in CrOCl

To investigate the magnetism in these thin CrOCl layers, we performed additional Scanning Nitrogen Vacancy Magnetometry (SNVM) measurements, presented in Figure S13 of the supplementary file. This technique utilizes an AFM tip integrated with a single NV center acting as a highly sensitive magnetic sensor, with its spin states being optically read out using laser and microwave radiation. Through this method, we were able to detect the weak antiferromagnetic field. However, we acknowledge that the technique is susceptible to environmental fluctuations, which, combined with the thinness of the CrOCl flakes, results in a modest signal-to-noise ratio. Despite this, the magnetic field scan in Fig. S13e clearly shows a discernible contrast difference. Additionally, figures S13a and S13b provide topographical and contrast data of the selected CrOCl flake, while Figures S13c and S13d present data obtained from ODMR (Optically Detected Magnetic Resonance) tuning.

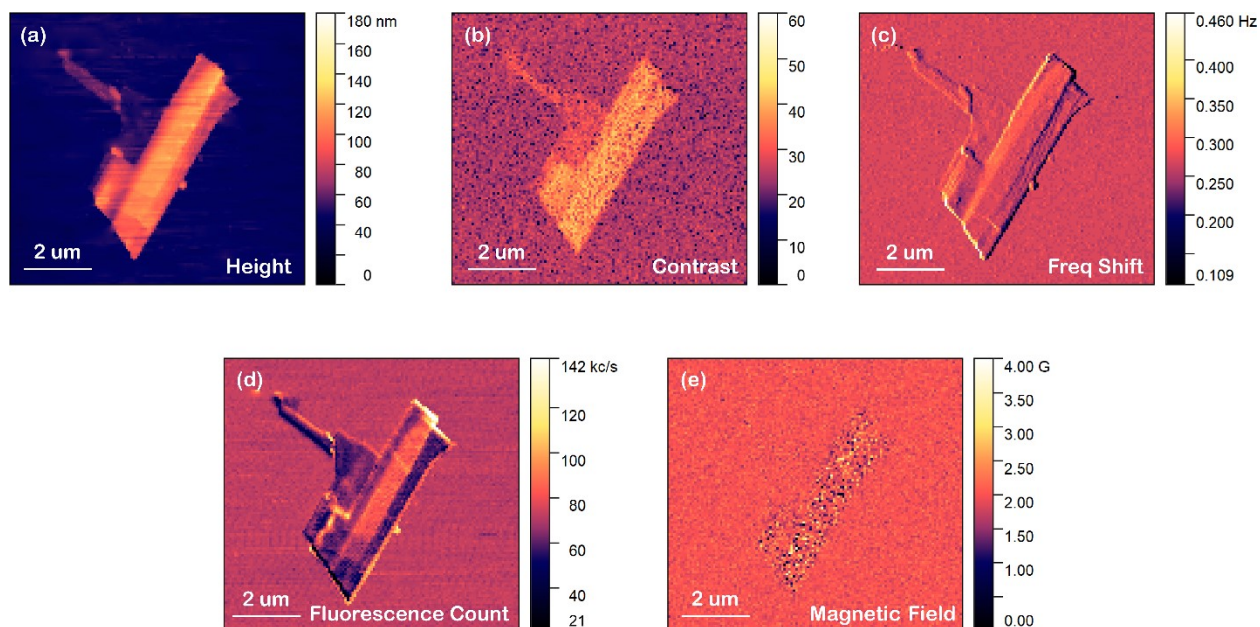


Figure S13: Scanning Nitrogen-Vacancy Magnetometry (SNVM) of CrOCl Flakes (a) Height Scan showing topography (b) Contrast Scan identifying thickness differences (c,d) Raw Frequency Shift and Fluorescence count for ODMR (Optically Detected Magnetic Resonance) (e) Magnetic Field scan identifying magnetism in these ultra-thin flakes

Furthermore, Vibrating Sample Magnetometry (VSM) measurements were conducted by stacking multiple substrates, as shown in Figure S14 of the supplementary file. The VSM results clearly reveal a paramagnetic-to-antiferromagnetic transition at the Néel temperature (~ 13.5 K), as indicated in Figures S14a and S14b. Since the samples were grown on substrates via CVD, the exact mass could not be determined, and magnetism is therefore reported in terms of magnetic moments rather than susceptibility.

Taken together, these new datasets provide compelling evidence of magnetism in the CrOCl flakes and confirm their antiferromagnetic nature.

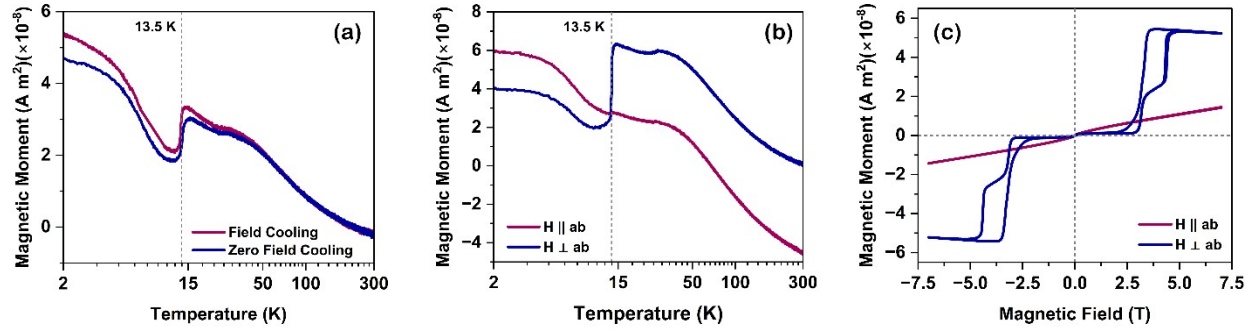


Figure S14: Vibrating Sample Magnetometry (VSM) of CrOCl (a) Moment vs Temperature curves of CrOCl in Field Cooled vs Zero Field Cooled configuration (b) Moment vs Temperature curves of CrOCl flakes in parallel vs perpendicular configuration in ZFC mode (c) Moment vs Field curves of CrOCl in parallel vs perpendicular configuration in ZFC mode